Advanced Ceramics Progress

Microwave-Assisted Solution Combustion Synthesis of WO₃ Nanoparticles: Optical and Colorimetric Characteristics

H. Aliasghari [a], A. M. Arabi [b] *, H. Haratizadeh [a] *

[a] Physics Department, Shahrood University of Technology, 3619995161, Shahrood, Iran
[b] Department of Inorganic Pigments and Glazes, Institute for Color Science and Technology (ICST), Tehran, Iran

ABSTRACT

Tungsten oxide (WO_3) and tungsten oxide hydrate ($WO_3.H_2O$) nanoparticles were synthesized via microwave-assisted solution combustion in comparison with the acidic precipitation method. Oxalic acid was used as a surfactant and forming agent in the acidic precipitation method. In addition to oxalic acid, glycine and citric acid were also used as fuels in the microwave-assisted combustion method. The synthesis process was investigated by thermogravimetric (TG) and Differential Thermal Analysis (DTA) analysis. The obtained nanoparticles were analyzed using the scanning electron microscopy (SEM) and X-ray diffraction (XRD) techniques. The sample synthesized via the acidic precipitation method showed an orthorhombic crystal structure. One of the samples synthesized via the microwave-assisted solution combustion method was monoclinic and the two others were amorphous. The acidic precipitation method resulted in uniform plate-like structures while the combusted samples indicated irregular spherical morphology. Fourier-transform infrared (FTIR) analysis revealed stretching-vibrating bands relating to W-O bonds in the synthesized tungsten oxide nanoparticles. The bandgap energy of the nanoparticles calculated using UV-Vis spectra and Tauc plot extrapolation increased with decreasing the particle size. The data of reflectance and colorimetry had good agreement with the maximum peak position in the absorption spectra. The results indicated that the acidic precipitation method controls the particle's morphology as well as the size distribution. Although the combustion of fuels releases a lot of heat, the synthesis by solution combustion can control the size and shape of the nanoparticles, which can be an appropriate method for mass production of nanoparticles.

1. INTRODUCTION

Transition metal oxides have attracted the attention of researchers due to their high-temperature stability, controllable mechanical, and electronic properties as well as photonic and electronic transitions [1,2]. Tungsten oxide can tolerate low pH values and have promising physical and chemical properties, which can be used in electrochromic [3], photochromic [4], photocatalytic [5], and gas sensing [6] applications that is an n-type intrinsic semiconductor with 2.6-3.6 eV bandgap, which can be modified through doping or manipulation [1,2]. Phase transitions from monoclinic II (ε-WO_3, <−43°C) to triclinic (δ-WO_3, −43 to 17°C), monoclinic I (γ-WO_3, 17–330°C), orthorhombic (β-WO_3, 330–740°C), and tetragonal (α-WO_3,> 740°C) occur in tungsten oxide through increasing the temperature under the ambient pressure [1,2,7]. Phase

transitions in nanomaterials can be completely different from those in bulk counterparts and depend mostly on the morphology and the crystal structure (i.e. the synthesis method). Tungsten oxide has a perovskite-type structure and its phase classification is performed according to the distortion angels and rotation direction of WO_6 octahedrons relative to the ideal ReO_3 cubic structure [1,2]. Tungsten oxide (WO_3) and tungsten oxide hydrate ($WO_3.H_2O$) nanostructures have been synthesized via different experimental procedures including aqueous sol-gel [8], acidic precipitation [9] hydrothermal [10], sputtering [11], etc. The synthesis methods should have the ability to control the morphology and crystal structure of the nanoparticles because the shape, size, and crystal structure of tungsten oxide nanoparticles significantly affect its electrical, magnetic, and optical properties [12]. Moreover, the large scale and cost-effective synthesis

*Corresponding Author Email: aarabi@icrc.ac.ir (A. M. Arabi), hamid.haratizadeh@gmail.com (H. Haratizadeh)

methods are required for industrial applications. In wet chemical methods, the morphology and crystal structure are controlled by using surfactants and reducing the surface energy of the particles [13]. The particle's morphology and size distribution are usually homogenous because closed and homogenous media are used in the wet chemical methods, which in fact, is not suitable for mass production. In contrast, the combustion method yields large quantities of the products in shorter times, but it is more difficult to control the morphology in the combustion method because of its higher reaction rate and temperature than wet chemical methods.

The Self-propagating High-temperature Synthesis (SHS) method was first introduced by Merzhanov et al., which is a high-temperature solid-state combustion method and results in coarser particles [14]. Patil et al. innovated the Solution Combustion Synthesis (SCS) method in which the combustion starts from a metal nitrate solution and the size and morphology of the particles are controllable by altering the combustion fuel [15].

The purpose of this reseach is to synthesize tungsten oxide (WO₃) and tungsten oxide hydrate (WO₃.H₂O) nanoparticles via the acidic precipitation and a novel microwave-assisted solution combustion synthesis method. Different morphologies and crystal structures were obtained based on the applied method and fuel.

2. EXPERIMENTAL PROCEDURES

All the chemicals were purchased and used without further purification. Tungsten metal powder (analytical grade, 99.99%) was purchased from Sigma Aldrich. Sodium tungstate ($Na_2WO_4.2H_2O$, >99%), HCl (30%), hydrogen peroxide (H_2O_2, 30%), HNO_3 (67%), H_2SO_4 (37%), oxalic acid ($C_2H_2O_4$, >99%), glycine ($C_2H_5NO_2$, >99%), and citric acid ($C_6H_8O_7$, >99%) were provided from Merck.

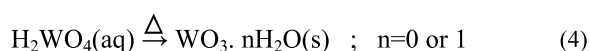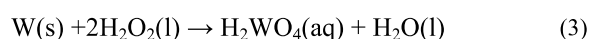### 2.1. Acidic Precipitation

Sodium tungstate dihydrate ($Na_2WO_4.2H_2O$) was dissolved in 50mL deionized water to obtain a transparent solution (0.5M). The same molar ratio of HCl was added into the solution under magnetic stirring as the sodium tungstate until light yellow precipitates appeared. Then, the reaction vessel was transferred into the oil bath of 90°C. Oxalic acid was subsequently added into the reaction system with the sodium tungstate solution/oxalic acid (W/C) ratio of 1:1.6. The final yellow precipitates of $WO_3.H_2O$ nanoplates were washed with deionized water and air-dried at 60°C. $WO_3.2H_2O$ first forms under the acidic condition, and then, transforms to $WO_3.H_2O$ in the presence of oxalic acid according to reaction (1) and (2) [16,17]:

$$WO_4^{2-} + 2H^+ + H_2O \rightarrow WO_3. 2H_2O \qquad (1)$$

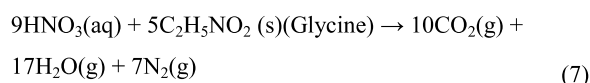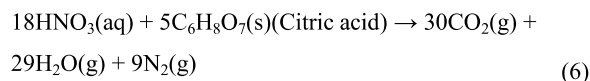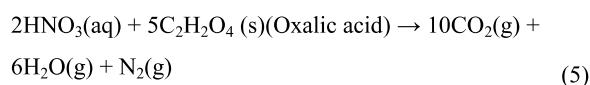$$WO_3. 2H_2O \rightarrow WO_3. H_2O + H_2O \qquad (2)$$
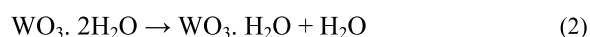
2.2. Microwave-Assisted Solution Combustion Synthesis

Tungsten oxide nanoparticles synthesis by microwave-assisted solution combustion was done through two simultaneous processes [18]. In this method, the tungstic acid was formed through reactions (3) and (4):

$$W(s) +2H_2O_2(l) \rightarrow H_2WO_4(aq) + H_2O(l) \qquad (3)$$

$$H_2WO_4(aq) \overset{\Delta}{\Rightarrow} WO_3. nH_2O(s) \ ; \ n=0 \text{ or } 1 \qquad (4)$$

The tungsten powder (4.0gr) was dissolved in a certain amount of H_2O_2 to obtain a transparent solution through Equation (3). In parallel, a combustion reaction produce the required heat (Δ) for the synthesis of tungsten oxide and the formation of the final structure. The combustion reaction is theoretically described based on the propellant chemistry and stoichiometric amounts of the reactants according to reactions (5) to (7) [19,20]:

$$2HNO_3(aq) + 5C_2H_2O_4 (s)(\text{Oxalic acid}) \rightarrow 10CO_2(g) + 6H_2O(g) + N_2(g) \qquad (5)$$

$$18HNO_3(aq) + 5C_6H_8O_7(s)(\text{Citric acid}) \rightarrow 30CO_2(g) + 29H_2O(g) + 9N_2(g) \qquad (6)$$

$$9HNO_3(aq) + 5C_2H_5NO_2 (s)(\text{Glycine}) \rightarrow 10CO_2(g) + 17H_2O(g) + 7N_2(g) \qquad (7)$$

Typically, 9.0mL nitric acid and 7.5gr citric acid ($C_6H_8O_7$) was introduced to the tungsten solution. After heating the solution on a hotplate at 80°C, the obtained viscous gel was transferred to a microwave oven (rotating sample at 900 watts) to complete the one-step combustion reaction in 60s . The same procedure was used for oxalic acid and glycine fuels. The samples were named WO, MO, MC, and MG according to Table 2. The combustion of all the fuels was done with flame in the microwave oven.

2.3. Characterization

Thermal analysis was carried out using a thermogravimetric analyzer (PYRIS DIAMOND) under the air atmosphere. The samples were placed in an open Al pan and heated from room temperature to a maximum temperature of 600°C at a rate of 10°C.min⁻¹. The crystal structure of the synthesized samples was examined by X-ray powder diffraction using a

PHILIPS-PW1730 X-ray diffractometer with Cu-Kα radiation (λ=1.54056Å) at 2θ range of 10-80 degree and step size of 0.02 degree. The SEM image (LEO 1455 VP apparatus) was used to determine the surface morphology of the nanoparticles. The information on the functional group and bonding of samples were provided by Fourier-transform infrared (FTIR) spectroscopy using a Perkin-Elmer spectrometer in a KBr matrix. The UV-Vis spectra for the powder samples were recorded at room temperature with a double beam (Perkin Elmer UV-Vis Lambda 20) spectrophotometer over the wavelength range of 200-800nm. The reflectance spectra of synthesized samples were measured by an xrite i1Pro 2 spectrophotometer in the wavelength range of 380-730nm.

3. RESULTS AND DISCUSSION

3.1. Theoretical Combustion Thermodynamics
In general, the formation of crystal structure, agglomeration, and particle growth and the final state of the system highly depends on the combustion reaction enthalpy, which is calculated according to the heat produced by the combustion of the fuels [15,21]. In an adiabatic system, the reaction heat is used to increase the reaction temperature. Therefore, the maximum reaction temperature T_{ad} is calculated through Equation (8) [15,22,23]:

$$\Delta H^{Tad} = \int_{298}^{Tad} C_p dT \qquad (8)$$

Where ΔH^{Tad} is the reaction enthalpy at T_{ad} and C_p is the specific heat capacity of the products. The theoretically calculated thermodynamic values for different fuels are listed in Table 1. The amount of exhaust gases during the combustion reaction affects

the porosity of the final product. The amount of the exhaust gases from reactions (5), (6), and (7) is 25, 68, and 34mol, respectively. The combustion heat of these reactions is -826kJ.mol^{-1}, -7364kJ.mol^{-1}, and -3539kJ.mol^{-1} which, results in the increase of the T_{ad} temperature to 1025.8K, 2526.7K, and 2438.2K, respectively by considering the amount of the exhaust gases. According to the amount (mol) of the reactants in reactions (5), (6) and (7), the oxidizer to fuel ratio was 0.4, 3.6, and 1.8, respectively.

3.2. Thermal Analysis
The combustion precursors were characterized by using thermogravimetry (TG), differential thermal analysis (DTA) to obtain a better understanding of the auto-combustion process. TG and DTG curves were obtained, however, a mass spectrometer was not available for the analysis of evolved gases. Generally, the DTA profile can be identified with four different stages for a SCS precursor: (a) endothermic loss of water, (b) combustion reaction, (c) removal of carbonaceous materials, and (d) final product formation with constant mass [24].

TABLE 1. Theoretically calculated thermodynamic values for different fuels

Fuel	Oxalic acid ($C_2H_2O_4$)	Citric acid ($C_6H_8O_7$)	Glycine ($C_2H_5NO_2$)
$\Delta H^0_{combustion}$ (kJ/mol)	-826	-7364	-3539
Oxidizer to fuel ratio	0.4	3.6	1.8
amount of exhaust gases (mol)	25	68	34
T_{ad} (K)	1025.8	2526.7	2438.2

Figures 1(a) and (b) illustrate the TG-DTG and DTA analysis results of the MO sample, respectively.
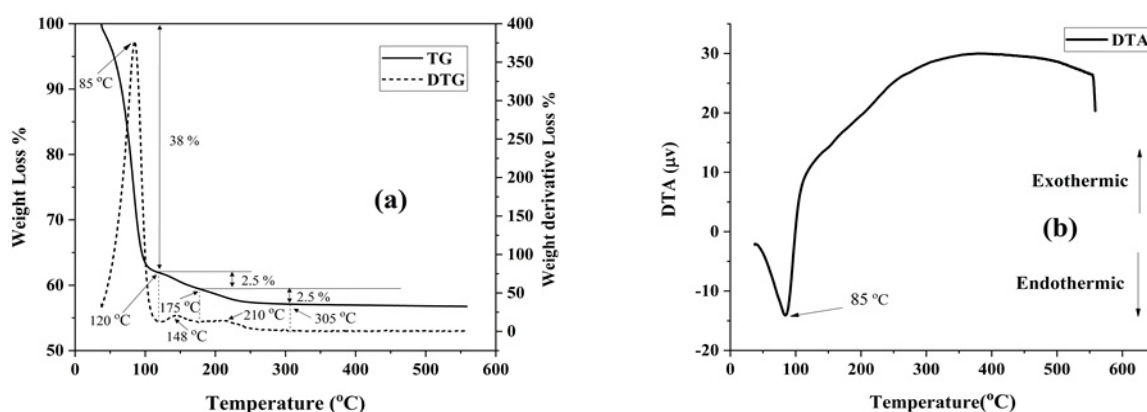

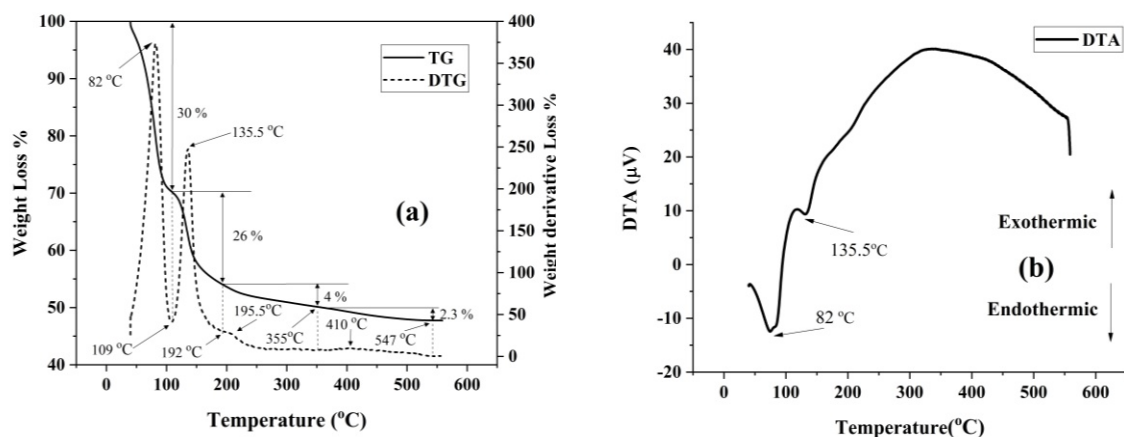**Figure 1.** (a) TG-DTG and (b) DTA analysis of MO sample

Figure 2. (a) TG-DTG and (b) DTA analysis of MC sample

and exothermic over 100°C (Figure 1a). The first weight loss was observed at 85°C in TG analysis. Nevertheless, it can be safely assumed that it corresponds to the removal of weakly absorbed water from the external surface of the prepared gel due to the low temperature of this feature. The exothermic nature of the weight loss over the 100°C can be assigned to the decomposition of oxalic acid that released the CO_2 and H_2O during the combustion of oxalic acid by nitric acid [25,26].

The combustion behavior of the MC sample was studied by TG-DTG and DTA, and the results are shown in Figures 2(a) and (b). The first endothermic peak at 82°C can be assigned to the evaporation of the remaining water in the gel and the other weak weight loss at 135.5°C arises from desorption of chemically absorbed [27]. A broad exothermic peak is observed between 100°C and 600°C, accompanied by a weight loss of about 32%, which is assumed to correspond to the combustion process of citric acid and exit of residuals [23,24,28].

The results of TG-DTG and DTA of combustion reaction for producing the MG sample are exhibited in Figures 3(a) and (b), respectively. As can be observed in the DTA graph, the reaction has an exothermic peak at 137 that can be attributed to the solution of glycine that forms the amine and carboxyl groups by an endothermic peak at 154. The abrupt weight loss at 100-300 shows the exothermic peak at 197 that can be corresponded to the combustion of glycine and decomposition of the carboxyl group and exiting the adsorbed water. While the combustion of glycine has a broad peak from 100-600, the second sharp exothermic peak is seen at 528 that can be attributed to the decomposition of the amine group of glycine [23,24,28].

The results indicate that glycine combustion is more severe than citric acid and oxalic acid. Although thermodynamic calculations show high-temperature production rates, however, it produces relatively low temperature combustion as the reaction proceeds from the soluble state, which results in the production of nanoparticles.
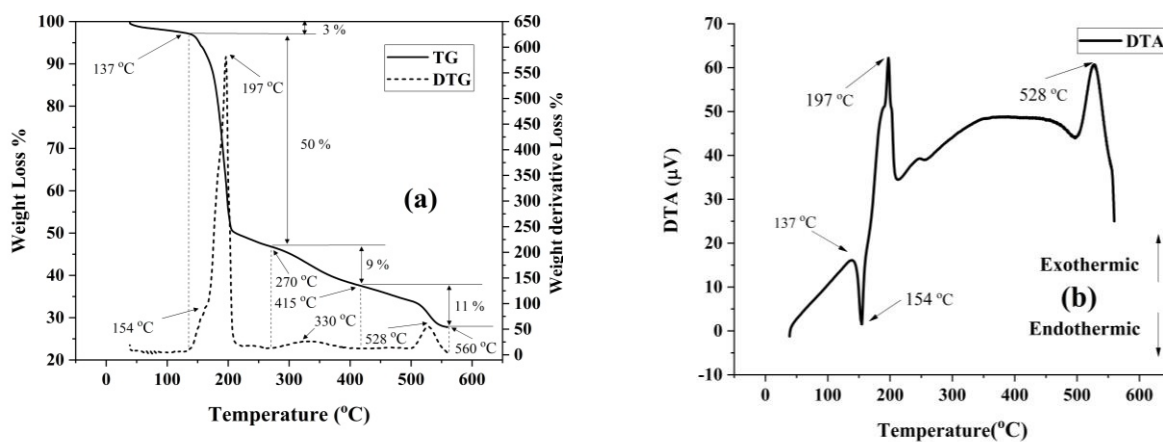

Figure 3. (a) TG-DTG and (b) DTA analysis of MG sample

3.3. Crystal Structure

XRD patterns of the synthesized samples are shown in Figure 4. The sample synthesized via acidic precipitation using oxalic acid contains fully crystallized orthorhombic tungsten oxide hydrate ($WO_3.H_2O$) nanoparticles according to JCPDS card no. 01-084-0886 [16,29]. The crystallite sizes of the samples calculated based on Scherrer in Equation (9) are listed in Table 2.

$$D = 0.9\, \lambda\, /\, \beta \cos\theta \qquad (9)$$

Where D is the crystallite size, λ is the wavelength of the incident radiation CuKα line, θ is the Bragg's angle, and β is the full width in half maximum (FWHM) [30].
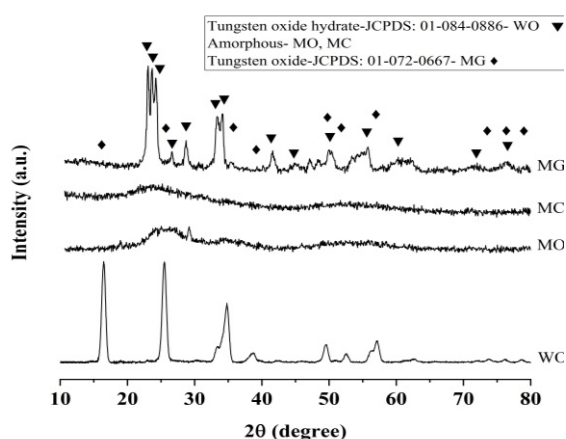

Figure 4. XRD patterns of WO, MO, MC, and MG samples

Microwave-assisted combustion synthesis in the presence of oxalic acid and citric acid has resulted in amorphous nanoparticles. It seems that there has not been enough time for MC and MO samples to crystallize because of the high intensity as well as the combustion reaction rate. The XRD pattern of the MG sample shows monoclinic tungsten oxide (WO_3) according to JCPDS card no. 01-072-0667. This difference in crystallization can be due to the higher reaction heat in the case of glycine fuel and the formation of amine groups during the reaction.

TABLE 2. Summary of synthesis method parameters and crystal structure of the synthesized nanoparticles

code	Synthesis method	Heat source	Fuel - Surfactant	Structure - JCPDS no	Crystallite size (nm)
WO	acidic precipitation	Heater	Oxalic acid	Orthorhombic 01-084-0886	13.9 nm
MO	Combustion	Microwave	Oxalic acid	Amorphous	-
MC	Combustion	Microwave	Citric acid	Amorphous	-
MG	combustion	Microwave	Glycine	Monoclinic 01-072-0667	23.7 nm

The needed temperature to the orthorhombic structure crystallization is 330-740°C, while the XRD pattern of the WO sample revealed the used temperature in the presence of oxalic acid has been reduced to about 90°C.

3.4. FTIR spectra

All peaks of samples have corresponded to their band assignment in Table 3 as band positions. There are obvious differences in the FTIR spectra of the synthesized samples. As can be seen from Figure 5, unlike amorphous samples, the crystalline samples show distinct peaks at different wavelengths. Peaks at $1650 cm^{-1}$ and $3400 cm^{-1}$ are related to the O-H bond, which has a higher intensity in MO and MC samples in comparison with MG and WO samples [31]. This is indicative of more water adsorption in MO and MC samples. Peaks in the range of $500-1000 cm^{-1}$ are attributed to different bonds between oxygen and tungsten; mostly belong to stretching-vibrating bands in WO_6 octahedral structures [18]. Some obvious differences in FTIR spectra of MG and WO samples are more broad peaks at $1650 cm^{-1}$ and $3400 cm^{-1}$, peak shift from $800 cm^{-1}$ to $650 cm^{-1}$ in WO sample, the appearance of a peak at $1000 cm^{-1}$, and disappearing of peaks at $1100 cm^{-1}$ and $1500 cm^{-1}$ [21-24].

TABLE 3. Band positions of FTIR spectra

Sample by band position (cm^{-1})				Band assignment	References
WO	**MO**	**MG**	**MC**		
3368	3501	3428	3206	υ_{sym} and υ_{asym} of OH	[31]
	2850		2916	υ_{sym} and υ_{asym} of (CH$_2$)	[32,33]
	1688		1711	υ_{asym} (COO)	[31]
1615	1688	1627		δ (H–O–H)	[31,33,34]
	1442	1410	1393	δ (CH$_2$)	[32]
	1251		1175	υ_{sym} (COO)	[31]
	1123	1079	1077	υ (W–O–C)	[31]
939			981	υ (W=O)	[31,33,34]
			888	υ (O–O) and υ (W–O$_{inter}$–W)	[33,35]
	820	814	794	υ (W–O$_{intra}$–W)	[33,35]
721	723			υ (O–W)	[35]
672	603			υ_{asym} (W–O)	[34]

3.5. Microstructure and Morphology

All WO yellow powder contained plate-like particles with cubic shapes due to the presence of oxalic acid as

a surfactant (Figure 6). According to SEM images, the plates are rather uniform in length, width, and height (about 100nm in thickness), which demonstrates the capability of acidic precipitation method for high accurate controlling of the morphology.
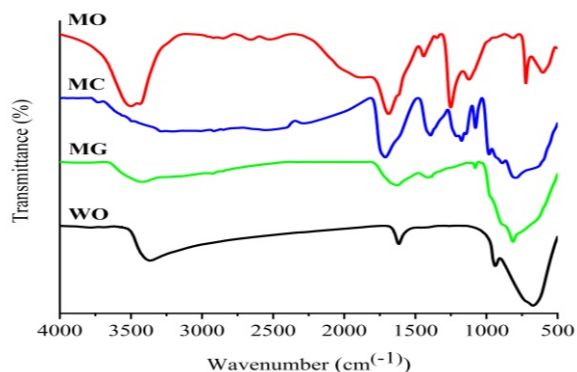

Figure 5. FTIR spectra of WO, MO, MC and MG samples

The schematic structure of $WO_3.2H_2O$ is shown in Figure 7a. The layers of corner-sharing $WO_5(OH_2)$ octahedron and interlayer water built the $WO_3.2H_2O$ [16]. The octahedrons of $WO_5(OH_2)$ consists of four W–O bonds, one W=O bond, and one $W–OH_2$ (structural H_2O) [31,33,34].

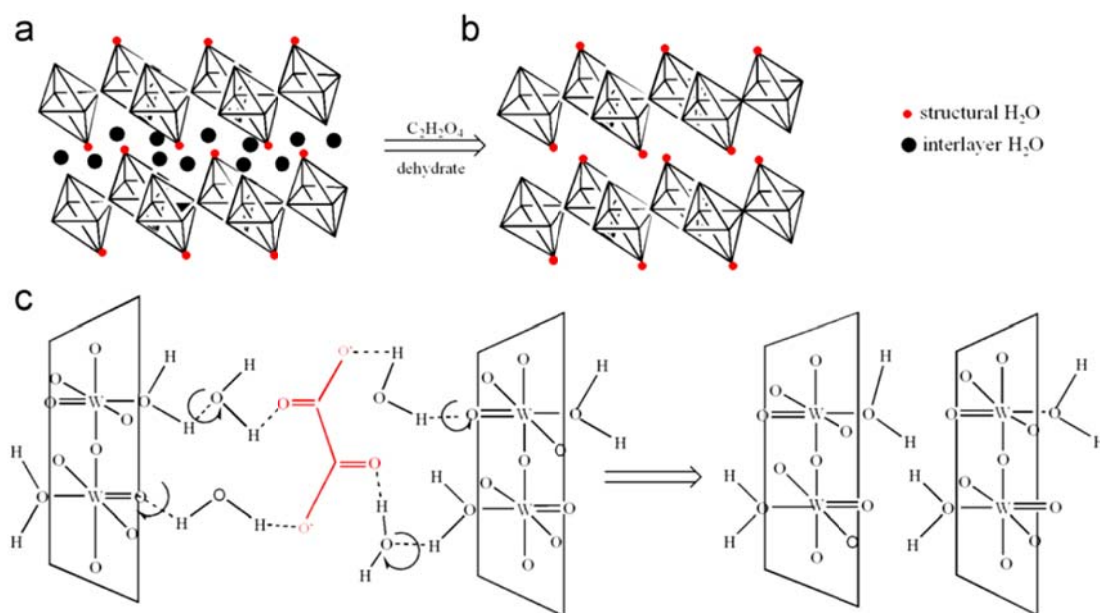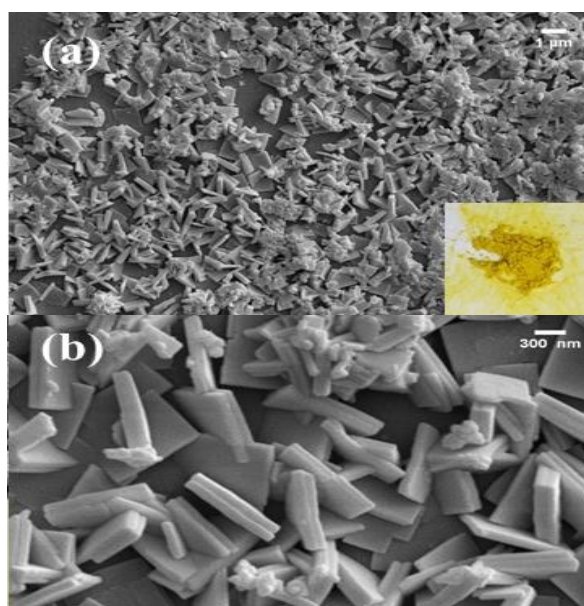**Figure 6.** SEM images of WO powder

Hydrogen bonds connect the interlayer water to $WO_5(OH_2)$ octahedron. Thus removal of interlayer water from $WO_3.2H_2O$ produces $WO_3.H_2O$ (Figure 7b) [16].

Figure 7. Schematic representation of (a) layered $WO_3.2H_2O$, (b) dehydrated $WO_3.H_2O$ from $WO_3.2H_2O$, and (c) the role of oxalic acid in dehydration process of $WO_3.2H_2O$ to $WO_3.H_2O$ [16]

The process is illustrated in Figure 7(a,b) in which $C_2H_2O_4$ destroyed the hydrogen bonds between the structural water and interlayer water. The electron-rich organic molecules of $C_2H_2O_4$ involve four O atoms that can form hydrogen bonds with four different interlayer H2O molecules in WO3.2H2O, as schematically shown in Figure 7c. The hydrogen bonds between interlayer water and $WO_5(OH_2)$ octahedron are destroyed by strong interactions of $C_2O_4^{2-}$ ions with interlayer water. Thus, $C_2H_2O_4$ plays

a key role in the dehydration process of $WO_3.2H_2O$ to $WO_3.H_2O$ at low temperatures (70-90°C) [16].

SEM images represent the nanoplates of WO were stacking side by side following the above-mentioned procedure. Unlike the WO sample, microwave-assisted synthesized samples showed irregular structures with less particle size than the WO sample (Figure 8). The MO powder is in yellowish-green and contains 50nm size particles with mostly spherical morphology. Black MC powder contained rock-like particles with irregular shape and size, which also confirms their amorphous nature as was shown in XRD patterns. MG sample is in navy blue and its SEM image shows spherical particles with a uniform particle size distribution of about 300nm. These differences in morphology are related to the applied materials and different synthesis methods. The results of TG-DTA analysis showed the intensity of the reaction, hence the final structure and morphology used in the combustion reaction depending on the fuel.
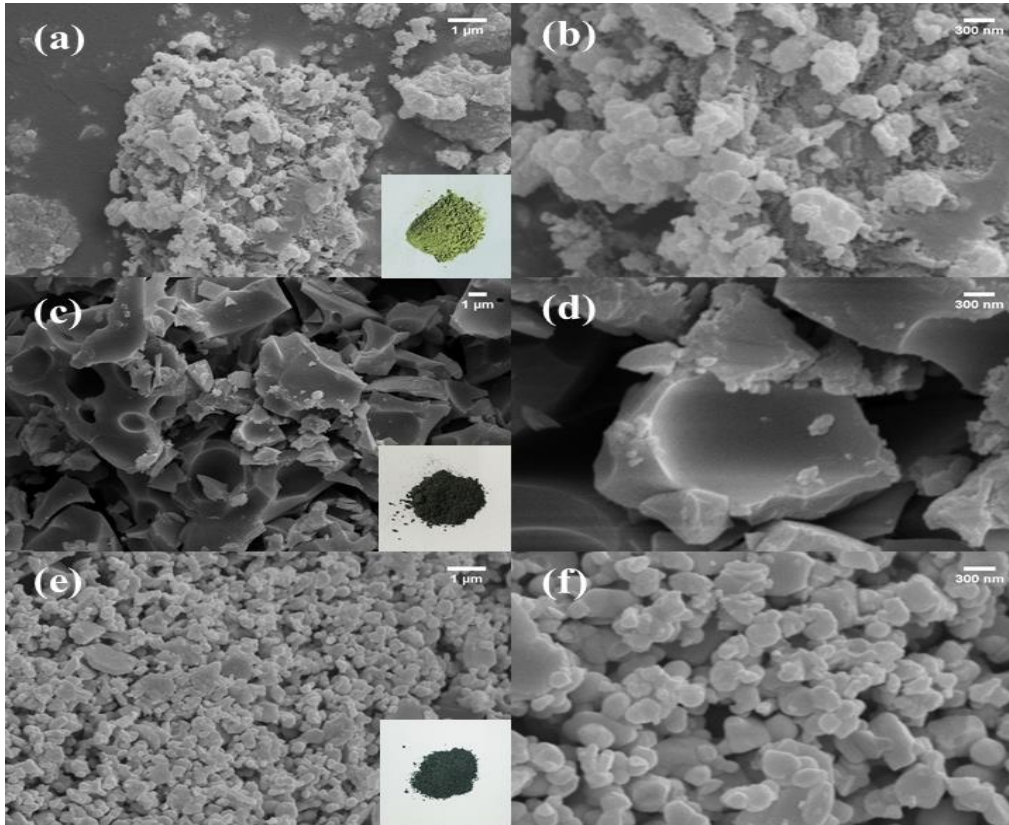

Figure 8. SEM images of (a, b) MO, (c, d) MC, and (e, f) MG samples

3.6. Optical Analysis and Band Gap

UV-Vis absorption spectra of the synthesized samples are shown in Figure 9. It can be seen that all the samples show adsorption edges at different wavelengths, which may arise from the quantum effects due to the size, crystal structure, and other influencing parameters. The bandgap was calculated according to the Tauc method by plotting $(\alpha h\upsilon)^{1/n}$ versus $h\upsilon$ using Equation (10):

$$(\alpha h\upsilon)^{1/n}=k(h\upsilon-E_g) \qquad (10)$$

Where h is the Planck constant, υ is the frequency of the incident photon, k is constant, α is the adsorption coefficient, and E_g is the bandgap energy [36,37].
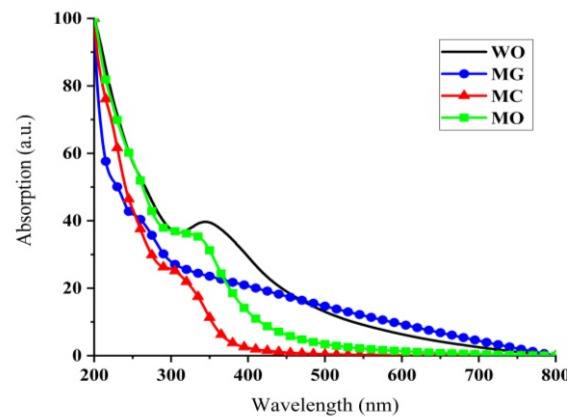

Figure 9. UV-Vis spectra of WO, MO, MC, and MG samples

Assuming a direct bandgap for synthesized nanoparticles, i.e. n=1/2, the bandgap is calculated by extrapolating the Tauc plot on the energy axis, as shown in Figure 10. It was observed that the band gaps were increased due to the quantum confinement effect arising from size reduction. The calculated band gaps for WO, MO, MC, and MG samples were 2.7, 3.2, 3.46, and 3.5eV, respectively.
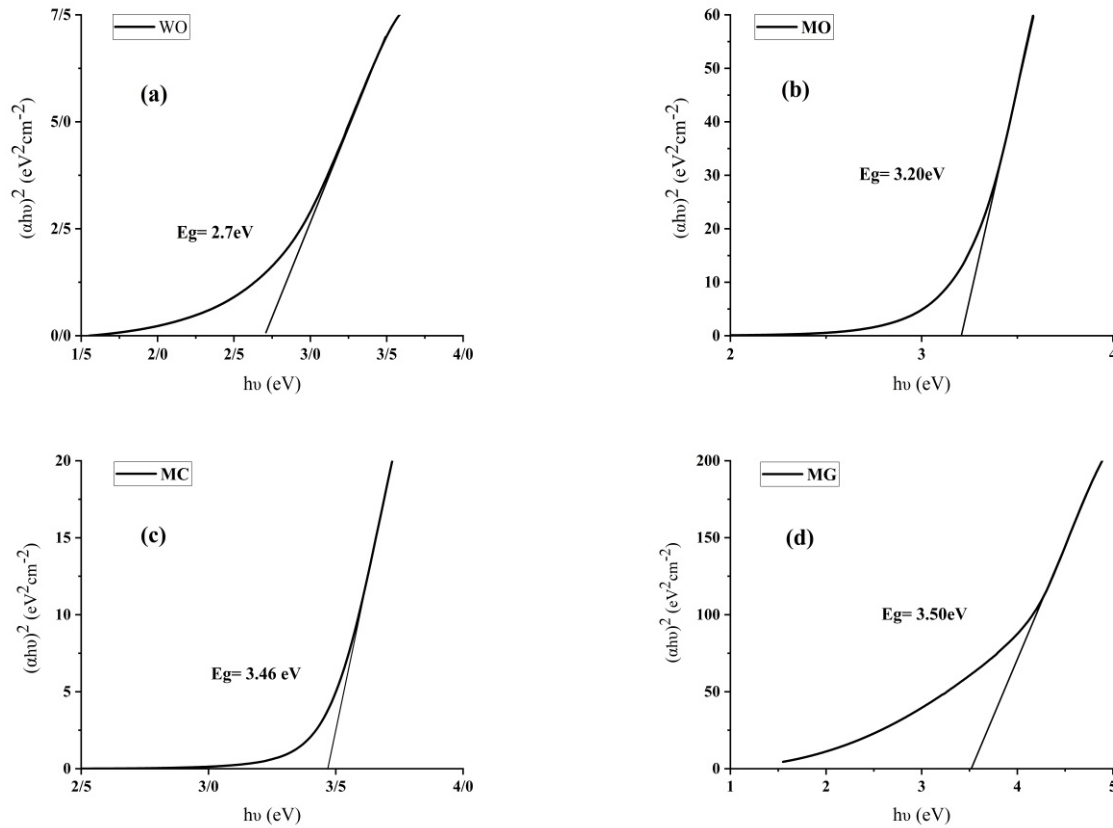

Figure 10. Tauc plot and bandgap calculation of (a) WO, (b) MO, (c) MC, and (d) MG samples

The CIE diagram of different samples is seen in Figure 11. The appearance of the samples is changed from the grey color of MG and MC samples to pale green in MO and greenish-yellow in WO samples. It seems that the black color of MG and MC samples is related to the residual carbonaceous matters from combustion reactions. There is a good agreement between the appearance of the samples (inset images of figures 7 and 8) and the colorimetric diagram.

The reflectance spectra of the samples are illustrated in Figure 12. There is also a good agreement between the appearance (Figure 11) and the visible reflectance of the samples. There is an obvious decrease in reflectance intensity because of the residual carbonaceous matters in MC and MG.

The maximum peak positions in the reflectance spectrum showed that the samples have absorption below 550nm, which illustrates the yellow color of samples with the various tendency to other colors.

The maximum peak position in the reflectance and absorption spectra is in good agreement with reflectance and shows the complementary absorption spectra.
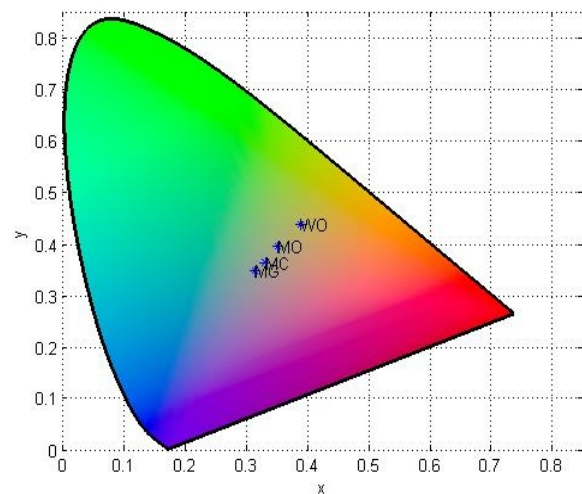

Figure 11. CIE diagram of WO, MO, MC, and MG samples

Moreover, the absorption edges illustrated by the rods in the figure have good compatibility with the Tauc formula.

It seems that the formation of crystalline WO_3 with maximum crystallite size of 24nm and maximum particle size of 300nm causes the quantum confinement and thus, increases the bandgap in comparison with the pure WO_3 sample (485nm) [28].

4. CONCLUSION

Acidic precipitation and microwave-assisted solution combustion methods were used for the synthesis of tungsten oxide hydrate ($WO_3.H_2O$) and tungsten oxide (WO_3) nanoparticles.

The particles showed orthorhombic, monoclinic, and amorphous structures. Thermodynamic calculations demonstrated that the fuels provide different reaction energies. Microwave-assisted combustion in the presence of oxalic acid yielded spherical particles while citric acid resulted in irregular shaped particles and glycine produced uniform fine spherical particles. Vibrating- stretching bands of W-O bonds in FTIR spectra also confirmed the formation of tungsten oxide. The influence of fuel type and synthesis method on the crystal structure can be obviously verified by the FTIR peaks in the range of $500\text{-}100 cm^{-1}$. The largest bandgap (3.5eV) calculated based on the Tauc relation as well as the adsorption and reflectance spectra belonged to the combustion in the presence of glycine fuel, which was about 1eV higher than the bulk WO_3, leading to the finest particle size. According to the results, the acidic precipitation method is suitable for morphology control while the combustion method can be used for mass production. CIE diagram showed that the WO sample has the purest yellow color. Purification can be done by sintering the microwave-synthesized samples at 400°C to remove the residual carbonaceous matters without any phase change. The SCS method can be assumed as a fast technique to mass production of nanoparticles.

REFERENCES

1. Zheng, H., Ou, J.Z., Strano, M.S., Kaner, R.B., Mitchell, A., Kalantar-zadeh, K., "Nanostructured tungsten oxide – properties , synthesis , and applications", *Advanced Functional Materials*, Vol. 21, No. 12, (2011), 2175–2196.

2. Cong, S., Geng, F., Zhao, Z., "Tungsten oxide materials for optoelectronic applications", *Advanced Materials*, Vol. 28, No. 47, (2016), 10518-10528.

3. Chang, X., Sun, S., Dong, L., Dong, Y., Yin Y., "Large-scale production of tungsten trioxide nanoparticles for electrochromic application", *RSC Advances*, Vol. 4, No. 18, (2014), 8994–9002.

4. Kumar, V.B., Mohanta, D., "Formation of nanoscale tungsten oxide structures", *Bulletin of Materials Science*, Vol. 34, No. 3, (2011), 435–442.

5. Rezaee, O., Mahmoudi Chenari, H., Ghodsi, F. E, "Precipitation synthesis of tungsten oxide nanoparticles: X-ray line broadening analysis and photocatalytic efficiency study", *Journal of Sol-Gel Science and Technology*, Vol. 80, No. 1, (2016), 109-118.

6. Liu, Z., Miyauchi, M., Yamazaki, T., Shen, Y., "Facile synthesis and NO_2 gas sensing of tungsten oxide nanorods assembled microspheres", *Sensors and Actuators B: Chemical*, Vol. 140, No.2, (2009), 514–519.

7. Thummavichai, K., Wang, N., Xu, F., Rance, G., Xia, Y., Zhu, Y., "In situ investigations of the phase change behaviour of tungsten oxide nanostructures", *Royal Society Open Science*, Vol. 5, No. 4, (2018), 171932.

8. Zhao, B., Zhang, X., Dong, G., Wang, H., Yan, H., "Efficient electrochromic device based on sol – gel prepared WO_3 films", *Ionics*, Vol. 21, No.10 (2015), 2879-2887.

9. Patil, V.B., Adhyapak, P. V., Suryavanshi, S.S., Mulla, I.S., "Oxalic acid induced hydrothermal synthesis of single crystalline tungsten oxide nanorods", *Journal of Alloys and Compounds*, Vol. 590, (2014), 283-288.

10. Ahmadi, M., Younesi, R., Guinel, M.J., "Synthesis of Tungsten Oxide Nanoparticles using a Hydrothermal Method at Ambient Pressure", *Journal of Materials Research*, Vol. 29, No. 13, (2014), 1424-1430.

11. Park, Y., Hong, Y., Lee, K., "Characterization of electrochromic WO_3 thin films fabricated by an RF sputtering method", *Journal of Ceramic Processing Research*, Vol. 14, No. 3, (2013), 337-341.

12. Migas, D.B., Shaposhnikov, V.L., Rodin, V.N., Borisenko, V.E., "Tungsten oxides . I . Effects of oxygen vacancies and doping on electronic and optical properties of different phases of WO_3", *Journal of Applied Physics*, Vol. 108, No. 9 , (2010), 093714.

13. Jiayin, L., Jianfeng, H., Jianpeng, W., Liyun, C., Yanagisawa, K., "Morphology-controlled synthesis of tungsten oxide hydrates crystallites via a facile, additive-free hydrothermal process", *Ceramics International*, Vol. 38, No. 6, (2012), 4495–4500.

14. Sharma, P., Lotey, G.S., Singh, S., Verma, N.K., "Solution-combustion: the versatile route to synthesize silver nanoparticles", *Journal of Nanoparticle Research*, Vol. 13, No. 6, (2011), 2553–2561.

15. Patil, K.C., "Advanced ceramics: Combustion synthesis and properties", *Bulletin of Materials Science*, Vol. 16, No. 6, (1993), 533–541.

16. Li, L., Zhao, J., Wang, Y., Li, Y., Ma, D., Zhao, Y., Hou, S., Hao, X., "Oxalic acid mediated synthesis of $WO_3.H_2O$ nanoplates and self-assembled nanoflowers under mild conditions", *Journal of Solid State Chemistry*, Vol. 184, No. 7, (2011), 1661–1665.

17. Ali Asghari, H., Aarabi, A. M., Haratizadeh, H., "Synthesis of Nanostructured Tungsten Oxide Thin Film", *The 7th International Color & Coating Congress (ICCC2017)*, Amirkabir University of Technology, Tehran, (2017).

18. Aliasghari, H., Arabi, A.M., Haratizadeh, H., "A novel approach for solution combustion synthesis of tungsten oxide nanoparticles for photocatalytic and electrochromic applications", *Ceramics International*, Vol. 46, No. 1, (2020), 403-414.

19. Nayak, A.K., Sohn, Y., Pradhan, D., "Facile green synthesis of $WO_3·H_2O$ nanoplates and WO_3 nanowires with enhanced photoelectrochemical performance", *Crystal Growth & Design*, Vol. 17, No. 9, (2017), 4949–4957.

20. Breedon, M., Spizzirri, P., Taylor, M., du Plessis, J., McCulloch, D., Zhu, J., Yu, L., Hu, Z., Rix, C., Wlodarski, W., Kalantar-zadeh, K., "Synthesis of nanostructured tungsten

oxide thin films: a simple , controllable , inexpensive , aqueous sol - gel method", *Crystal Growth & Design*, Vol. 10, No. 1, (2010), 430-439.

21. Khodadadi, M.R., Olya, M.E., Naeimi, A., "Highly efficient Al-doped ZnO:Ag catalyst for RB19 photocatalytic degradation: Microwave-assisted synthesis and characterization", *Korean Journal of Chemical Engineering*, Vol. 33, No. 7., (2016), 2018-2026.

22. Ahmadian, H., Al. Hessari, F., Arabi, A.M., "Preparation and characterization of Luminescent nanostructured Gd_2O_3-Y_2O_3:Eu synthesized by the solution combustion process", *Ceramics International*, Vol. 45, No. 15., (2019), 18778-18787.

23. Chen, P., Qin, M., Chen, Z., Jia, B., Qu, X., "Solution combustion synthesis of nanosized WO_x: Characterization, mechanism and excellent photocatalytic properties", *RSC Advances*, Vol. 6, No. 86, (2016), 83101–83109.

24. Hossain, M.K., Kecsenovity, E., Varga, A., Molnár, M., Janáky, C., Rajeshwar, K., "Solution combustion synthesis of complex oxide semiconductors", *International Journal of Self-Propagating High-Temperature Synthesis*, Vol. 27, No. 3, (2018), 129–140.

25. Higgins, J., Zhou, X., Liu, R., Huang, T.T.S., "Theoretical study of thermal decomposition mechanism of oxalic acid", *The Journal of Physical Chemistry A*, Vol. 101, No. 14, (1997), 2702–2708.

26. Kakumoto, T., Saito, K., Imamura, A., "Unimolecular decomposition of oxalic acid", *Journal of Physical Chemistry*, Vol. 91, No. 9, (1987), 2366–2371.

27. Raudoniene, J., Laurikenas, A., Kaba, M.M., Sahin, G., Morkan, A.U., Brazinskiene, D., Asadauskas, S., Seidu, R., Kareiva, A., Garskaite, E., "Textured WO_3 and WO_3: Mo films deposited from chemical solution on stainless steel", *Thin Solid Films*, Vol. 653, (2018), 179–187.

28. Liu, Y., Li, B., Wei, X., Pan,W., "Citric-nitrate combustion synthesis and electrical conductivity of the Sm^{3+} and Nd^{3+} co-doped ceria electrolyte", *Journal of the American Ceramic Society*, Vol. 91, No. 12, (2008), 3926–3930.

29. Miao, B., Zeng, W., Lin, L., Xu, S., Ding, X., "Syntheses and mechanism of $WO_3 \cdot H_2O$ nanoflowers assembled of square nanoplates with the assistance of oxalic acid", *Nanoscience and Nanotechnology Letters*, Vol. 5 , No.7 (2013), 765–769.

30. Rajeshwar, K., De Tacconi, N.R., "Solution combustion synthesis of oxide semiconductors for solar energy conversion and environmental remediation", *Chemal Society Review*, Vol. 38, No. 7, (2009), 1984–1998.

31. Sharma, N., Deepa, M., Varshney, P., Agnihotry, S.A., "FTIR investigations of tungsten oxide electrochromic films derived from organically modified peroxotungstic acid precursors", *Thin Solid Films*, Vol. 401, No. 1-2, (2001), 45–51.

32. Yin, J., Cao, H., Zhang, J., Qu, M., Zhou, Z., "Synthesis and applications of γ-tungsten oxide hierarchical nanostructures", *Crystal Growth & Design*, Vol. 13, No.2, (2013), 759-769.

33. Djaoued, Y., Ashrit, P.V., Badilescu, S., Brüning, R., "Synthesis and characterization of macroporous tungsten oxide films for electrochromic application", *Journal of Sol-Gel Science and Technology*, Vol. 28, (2003), 235–244.

34. Solis, J.L., Hoel, A., Lantto, V., Granqvist, C.G., "Infrared spectroscopy study of electrochromic nanocrystalline tungsten oxide films made by reactive advanced gas deposition Infrared spectroscopy study of electrochromic nanocrystalline tungsten oxide films made by reactive advanced gas deposition", *Journal of Applied Physics*, Vol. 89, No. 5, (2001), 2727-2732.

35. Pang, H.F., Xiang, X., Li, Z.J., Fu, Y.Q. Zu, X.T., "Hydrothermal synthesis and optical applications and materials science properties of hexagonal tungsten oxide nanocrystals assisted by ammonium tartrate", *Physica Status Solidi (a)*, Vol. 209, No. 3, (2012), 537–544.

36. Murphy, A.B, "Band-gap determination from diffuse reflectance measurements of semiconductor films, and application to photoelectrochemical water-splitting", *Solar Energy Materials and Solar Cells*, Vol. 91, No. 14, (2007), 1326–1337

37. Madhavi, V . Kondaiah, P. Hussain, O.M., Uthanna, S., "Structural, optical and electrochromic properties of RF magnetron sputtered WO_3 thin films", *Physica B: Condensed Matter*, Vol. 454, (2014), 141–147.